# Enhancing electrochemical capacitor performance of N-doped tannin-derived carbons by hydrothermal treatment in ammonia

Oscar Pinto-Burgos, Jimena Castro-Gutiérrez, Po Shan Poon, Maria Izquierdo, Alain Celzard, Vanessa fierro, Juan Matos

## ▶ To cite this version:

Oscar Pinto-Burgos, Jimena Castro-Gutiérrez, Po Shan Poon, Maria Izquierdo, Alain Celzard, et al.. Enhancing electrochemical capacitor performance of N-doped tannin-derived carbons by hydrothermal treatment in ammonia. Journal of Power Sources, 2024, 602, pp.234332. 10.1016/j.jpowsour.2024.234332 . hal-04559743

**HAL Id: hal-04559743**
**https://hal.univ-lorraine.fr/hal-04559743v1**

Submitted on 25 Apr 2024

# Enhancing electrochemical capacitor performance of N-doped tannin-derived carbons by hydrothermal treatment in ammonia

Oscar Pinto-Burgos[a,b]*, Jimena Castro-Gutiérrez[c], Po Shan Poon[b], Maria T. Izquierdo[d], Alain Celzard[c,e], Vanessa Fierro[c]** Juan Matos[f]**

[a]Departamento de Ingeniería Química, Facultad de Ingeniería, Universidad de Concepción, Barrio Universitario s/n, Chile.

[b]Unidad de Desarrollo Tecnológico, UDT, Universidad de Concepción, Barrio Universitario s/n, Concepción, Chile.

[c]Université de Lorraine, CNRS, IJL, F-88000, Epinal, France.

[d]Instituto de Carboquímica (ICB-CSIQ), Miguel Luesma Castán 4, E-50018, Zaragoza, Spain.

[e]Institut Universitaire de France (IUF), 75005 Paris, France.

[f] Unidad de Cambio Climático y Medio Ambiente (UCCMA), Instituto Iberoamericano de Desarrollo Sostenible (IIDS), Facultad de Arquitectura, Construcción y Medio Ambiente, Universidad Autónoma de Chile, Temuco 4780000, Chile.

* Corresponding Author

** Corresponding Authors

E-mails addresses: oscpinto@udec.cl (O. Pinto-Burgos); juan.matos@uautonoma.cl (J. Matos); Vanessa.Fierro@univ-lorraine.fr (V. Fierro).

Phones: +56 9 78064083, +56 9 9379 8340, +33 (0)372 749 677

## Abstract

This study demonstrates that ammonia concentration when doping carbons using hydrothermal treatment has crucial impact on textural properties. The latter translates into an improvement of the electrochemical performance of carbon materials, when used into electrochemical capacitors, especially at high-rate performance. Nitrogen-doped carbons were synthesized by subjecting tannin to hydrothermal carbonization in ammonia solutions of varying concentrations. After carbonization and $CO_2$ activation, the as-produced activated carbons (ACs) were tested as electrodes for electrochemical capacitors in symmetric configuration using 1 M $H_2SO_4$ as aqueous electrolyte. Interestingly, ammonia concentration during the hydrothermal synthesis step did not significantly affect the final N content (ca. 3 and 4 at. %) nor the nitrogen and oxygen functionalities on the surface. However, the use of ammonia had crucial impact on the textural properties developed by $CO_2$ activation, and therefore on the electrochemical performance of the ACs. The best-performing N-doped AC showed specific electrode capacitance values, based on carbon material, of 212 $F \cdot g^{-1}$ at 0.5 $A \cdot g^{-1}$ and outstanding capacitance retention of ca. 71 % at 40 $A \cdot g^{-1}$. It also showed high cycling stability, with capacitance retention of ca. 96 % after 30,000 cycles. Furthermore, this AC outperformed similar reported materials, achieving a specific energy of 4.6 $W \cdot h \cdot kg^{-1}$ at 12.1 $kW \cdot kg^{-1}$.

***Keywords***: Tannin; Capacitance; Nitrogen doping; Carbon materials; Sustainable energy

## 1. Introduction

The increasing use of renewable energy sources, the rise of electromobility, and the advances in the development of wireless devices used in our daily lives have significantly contributed to the growing demand for efficient energy storage systems. Among these, electrochemical energy systems, such as batteries and electrochemical capacitors (ECs) have emerged as key components [1–3]. While batteries store energy by means of chemical reactions involving the transformation of chemical bonds through electrochemical redox reactions, ECs store charge by a physical process, namely the accumulation of electrostatic charge at the electrode/electrolyte interface [4,5]. As a result, the EC storage process is rapid and highly reversible, as it involves no chemical or phase change. Consequently, the charge/discharge cycle can be repeated over a long period with minimal impact on the performance of the electric device. Therefore, a major advantage of ECs is their extended lifespan, as they can withstand up to 20,000 charge-discharge cycles with a minor drop of less than 10 % in terms of performance retention. In contrast, batteries have a lifespan ranging from 500 to 3,000 cycles [6]. However, ECs suffer from a notable drawback: their low specific energy, which prevents them from storing large quantities of electrochemical energy when compared with batteries.

Since the early 2000s, the scientific community has devoted increasing efforts to improve the specific energy and power of ECs [1,7]. The forefront of research and development in this field has witnessed the adoption of several key approaches, namely: (i) tailoring the structure of electrode materials to optimize ion transport and adsorption according to electrolyte properties [8,9]; (ii) widening the potential window of the working cell using novel electrolytes [10,11]; and (iii) incorporating specific electroactive molecules to introduce redox contributions [12,13].

In this context, activated carbons (ACs) have been widely used as the main material for EC electrodes due to their ability to be tailored in terms of porosity and surface chemistry to meet specific requirements [14]. In addition, ACs can be synthesized from a variety of raw materials, including, but not limiting to, coals, petroleum coke, polymeric materials, and various forms of raw or waste biomass [15–18]. In particular, tannins, based on polyphenolic compounds often extracted from tree bark, have proven to be excellent precursors for the development of carbon-based electrodes for ECs [9,19–23]. Tannins indeed possess an excellent carbon yield, about 45 %, and an inherent ability for auto-condensation reactions, making them an attractive option for the production of high value-added materials [23,24]. Furthermore, the presence of -OH groups enables high reactivity, allowing the incorporation of other atoms or functionalities [22,25]. In this context, the amination of tannins using ammonia by hydrothermal carbonization (HTC) has been explored to achieve *in situ* N-doping [26].

Considering the amination of a single hydroxyl group in the flavonoid unit, the N content of tannin-derived materials should be 4.8 wt.% [25,26]. It is expected that tannin amination can proceed beyond the usual stoichiometry by subjecting it to an HTC process using concentrated ammonia solutions. However, most research using ammonia during the HTC step does not vary the ammonia concentration. On the other hand, to obtain optimal performance in ECs [27], the obtained materials need to be activated either by chemical activation (e.g. using KOH) or by physical activation (e.g. using $CO_2$). While the former results in ACs with higher surface areas [28], the latter enhances wettability and pore connectivity, leading to ECs with superior performance, particularly for high-power applications [29].

In this study, we focused on the synthesis of N-doped ACs derived from pine bark tannins, using ammonia solutions as hydrothermal medium. The resulting hydrochars were then carbonized and were physically activated using $CO_2$. This study is mainly concerned with the influence of N content on the textural and chemical surface properties after $CO_2$ activation and, ultimately, on their performance as electrodes for ECs.

## 2. Materials and methods

### 2.1 Synthesis of carbon materials

Ammonia solution ($NH_4OH$, 26.2 wt. % in water, Merck), sulfuric acid ($H_2SO_4$ 1M aqueous solution, Sigma Aldrich), polytetrafluoroethylene (PTFE, 60 wt. % suspension in water, Aldrich), carbon black powder (Sigma Aldrich), and glass fiber separator were used as received.

Tannins were obtained by water-ethanol extraction of *Pinus Radiata* bark from Chile [30]. They were dried, ground and sieved to obtain a roughly unimodal particle size distribution. In a first step, the tannins were subjected to HTC. In a typical synthesis, 1 g of tannin was added to 9 mL of ammonia solution with concentrations of ca. 1.6 wt. % or 3.2 wt. %. These values correspond to 4 and 8 mmol of nitrogen per gram of tannin, respectively. The solution was stirred for at least 15 min at room temperature, then subjected to HTC at 190 °C for 18 h. For comparison purposes, tannins-derived hydrochars were also prepared in distilled water. These materials were labelled as N4THC, N8THC and THC, respectively. The resulting hydrochars were washed with distilled water, dried under vacuum (80 °C, overnight), and pyrolyzed under $N_2$ flow (800 °C, 1 h, 10 °C $min^{-1}$). Finally, the pyrolyzed materials underwent $CO_2$ activation at 800 °C for 1, 2, and 4 h, and at 900 °C for 1, 1.5, and 2 h to obtain a wide range of burn-offs (BO). The temperature and time parameters used during the physical activation step were thus added to the aforementioned labels. For instance, N8THC900-1.5 is the AC obtained from N8THC after pyrolysis at 800 °C and additional $CO_2$ activation at 900 °C for 1.5 h.

## 2.2 Physicochemical characterization

The textural properties of the ACs were obtained from nitrogen and hydrogen adsorption-desorption isotherms at -196 °C acquired using a 3Flex equipment (Micromeritics). First, the Brunauer-Emmet-Teller area ($A_{\mathrm{BET}}$) was obtained from nitrogen adsorption isotherms following the IUPAC recommendations [31]. The Gurvich volume ($V_{0.97}$) was determined at a relative pressure ($P/P^{\circ}$) of 0.97. The non-local density functional theory kernel for heterogeneous surface (NLDFT-HS) with the parameter $\lambda = 3.2$ was also applied to $N_2$ and $H_2$ adsorption isotherms to estimate the pore size distribution (PSD). From the latter, specific surface area (SSA), total pore volume ($V_{\mathrm{T}}$), ultra-micropore volume ($V_{\mathrm{u\mu}}$, pore diameter below 0.7 nm), supermicropore volume ($V_{\mathrm{s\mu}}$, pore diameter between 0.7 and 2 nm), micropore volume ($V_{\mu} = V_{\mathrm{u\mu}} + V_{\mathrm{s\mu}}$) and mesopore volume ($V_{\mathrm{meso}} = V_{\mathrm{T}} - V_{\mu}$) were calculated. The choice of the $N_2$+$H_2$ adsorption isotherm combination instead of $N_2$+$CO_2$ was made to extend the lower limit value of the PSD and to prevent potential specific interactions between $CO_2$ and N-functional groups that that could lead to misleading textural characterization [32,33]. The average pore width ($\langle w \rangle$) for each range was calculated by Eq. (1):

$$\langle w \rangle = \frac{\sum_i \frac{dV}{dw_i} w_i \Delta w_i}{\sum_i \frac{dV}{dw_i} \Delta w_i} \tag{1}$$

Surface chemistry and the nature of oxygen and nitrogen functional groups were analyzed by X-ray photoelectron spectroscopy (XPS) using an OMICRON ESCAPlus system equipped with a non-monochromatized Mg Kα X-ray source (1253.6 eV). The C 1s, O 1s, and N 1s spectral regions were deconvoluted by assigning peaks based on Smith et al. [34] and Ayiania et al. [35] and fitting them with Gaussian-Lorentzian curves. Elemental analysis (C, N, H, and O) was carried out using a Vario EL Cube analyzer (Elementar). TEM images were acquired using TEM JEOL 1200 EXII equipment

## 2.3 Electrochemical characterization

Electrochemical characterization of the ACs as electrodes for ECs was conducted using a BioLogic VMP3 workstation with a symmetrical two-electrode configuration in a Swagelok cell. The electrode preparation involved an 85:10:5 weight ratio of carbon material, PTFE as binder, and carbon black as conductive additive, respectively. Ethanol was added to ensure homogeneity, and the resulting paste was dried overnight. Disc-shaped electrodes with a 5 mm diameter and a mass load close to 10 mg cm$^{-2}$ were cut from the paste. Prior to analysis, the electrodes were soaked in 1 M $H_2SO_4$ electrolyte for at least two days for impregnation. The electrochemical cell assembly consisted of gold current collectors, carbon electrodes and a porous quartz fiber separator, arranged from the outermost component towards the cell center. All components were immersed in the aqueous electrolyte.

Electrochemical impedance spectroscopy (EIS) measurements were performed by applying an alternating current at open circuit potential (OCP) over a frequency range from 100 kHz to 1 mHz with a sinusoidal amplitude of 10 mV. The data obtained were used to generate Nyquist and Bode plots. The bulk electrolyte resistance ($R_s$) and charge transfer resistance ($R_{CT}$) were calculated applying Eq. (1) in the high-frequency region [36], and the equivalent series resistance (ESR) was estimated using a linear line fit in the low-frequency region of the Nyquist plot [37].

$$\left(Z_r - R_s - \frac{R_{CT}}{2}\right)^2 + Z_i^2 = \left(\frac{R_{CT}}{2}\right)^2 \tag{1}$$

Cyclic voltammetry (CV) experiments were conducted using a 0 – 1 V potential window, with scan rates ranging from 5 to 1000 mV s$^{-1}$. The specific cell capacitance ($C_{CV,cell}$) was calculated using Eq. (2) where $I$ is the current, $v$ is the scan rate, $\Delta V$ is the potential window, and $m$ is the total mass of carbon used in both electrodes:

$$C_{CV,cell} = \frac{\int I dV}{v \, \Delta V \, m} \tag{2}$$

The collected CV data, obtained at different scan rates, were used to estimate electric double-layer capacitance ($C_{\mathrm{EDL}}$) and pseudo-capacitance ($C_{\mathrm{PsC}}$) contributions using Trasatti's method [38]. A brief description of this method is included in the supplementary material (SM).

Galvanostatic charge/discharge (GCD) cycling was also performed within the same 0 – 1 V potential window, applying a specific current from 0.5 to 40 A $g^{-1}$, based on the total mass of an electrode. The specific cell capacitance ($C_{\mathrm{GCD,cell}}$) was also determined from the GCD discharge curves using Eq. (3):

$$C_{GCD,cell} = \frac{I}{\left(\frac{dV}{dt}\right)m} \qquad (3)$$

where $I$ is the applied current, $m$ is again the total mass of carbon in the electrodes, and $dV/dt$ is the slope of the discharge curve in V $s^{-1}$. The $dV/dt$ slope was calculated in the range 0.4 – 1 V after subtraction of the corresponding potential drop ($iR$) [39,40]. The specific cell capacitances obtained from CV ($C_{CV,cell}$) and GCD ($C_{GCD,cell}$) are based on the carbon material. Additionally, to provide a basis for comparison, the specific capacitance of a single electrode ($C_{el}$) is calculated according to Eq. (4) [10]:

$$C_{el} = 4 \cdot C_{cell} \qquad (4)$$

which is valid for a symmetrical electrode configuration, where both electrodes are equal in terms of mass, thickness, size and material. The specific cell capacitances obtained from the GCD curves were used to calculate specific energy (E, in W·h $kg^{-1}$) and power (P, in W $kg^{-1}$) using Eq. (5) and (6), respectively:

$$E = \frac{1}{2\times3.6} C_{GCD,cell}\, V^2 \qquad (5)$$

$$P = 3600 \frac{E}{t_D} \qquad (6)$$

In these equations, the potential window is corrected by the corresponding $iR$ drop, and $t_D$ is the time required for complete discharge of the electrochemical cell.

## 3. Results and discussion

### 3.1 Chemical composition

The chemical composition of the ACs in the bulk and on the surface of the materials was obtained by elemental analysis and XPS, respectively. **Table S1** in supplementary material (SM) shows a summary of these results as a function of the burn-off (BO) used to obtain each AC. Elemental analysis of the materials revealed some notable features with increasing BO. For instance, the use of ammonia during the HTC step resulted in the incorporation of a very similar N content, 4.6 and 4.8 wt.% in N4THC and N8THC, respectively. The N content decreased after $CO_2$ activation to values of 3.0 – 3.7 wt.% for the N4THC-derived ACs, and 3.3 – 4.2 wt.% for the N8THC-derived ACs. An increase in O content was observed as well, with the undoped material exhibiting approximately 4.5 wt. %, while N4THC800 and N8THC800 had O contents close to 6.7 and 6.2 wt.%, respectively.

The C content in the bulk decreased after 4 h of activation with $CO_2$ at 800 °C. This decrease was more pronounced for N-doped samples, suggesting a catalytic effect during the activation process, which corresponds to the observed increase in BO for the samples subjected to 4 h $CO_2$ activation. In addition, these N-doped series exhibited a remarkable increase in O content, 13.2 and 13.1 wt.% for N4THC800-4 and N8THC800-4, respectively. Similarly, the series of carbons activated at 900 °C followed a similar trend, with a slight decrease in C content and increase in O content. In contrast, the non-activated N-doped samples (N4THC800 and N8THC800) showed a lower C content than the non-doped THC800 sample. Simultaneously, the O content increased both in the bulk material, according to elemental analysis, and at the surface, according to XPS analysis. As expected, the N content was noticeably higher in N-doped samples than in non-doped samples. However, the N content showed no significant differences between N4THC800 and N8THC800, either in bulk or in surface composition.

Due to the highly oxygen content in tannins, their carbonization results in a non-graphitizable carbon material [41]. Previous studies on tannin-derived carbon materials [19,20,42] have verified, through Raman spectra, the disordered nature of the carbon network in these materials, where the intensity of the D1 band is comparable to, or even greater than, that of the G band. A slight increase in the intensity ratio of the D and G bands is expected with $CO_2$ activation, along with a narrower D band [42], indicating that $CO_2$ tends to react with the most disordered or defective regions of the carbon network.

The XPS results presented in **Table S1** (SM) suggest that in the absence of N, the non-doped carbons (THC800 series) exhibited a similar surface chemical composition, i.e., C and O contents remained nearly the same, regardless of the BO, which increased from approximately 10 to 25 %. It is evident that the C content at the surface of the doped materials decreased compared to that of the THC800 materials due to the introduction of N functionalities by the amination process. The O content at the surface showed minimal variation between the non-doped and the two N-doped series, being slightly higher for materials derived from N8THC.

**Figure S1** in the supplementary material (SM) shows the XPS spectra of non-activated carbon materials, namely THC800, N4THC800, and N8THC800. The interpretation of the XPS spectra is based on previous studies [34,35,43], which provide valuable insights into this matter. For a detailed analysis of the relative atomic composition of the deconvoluted peaks in the C 1s, O 1s, and N 1s regions for tannin-derived carbons and N-doped tannin-derived carbons, please refer to **Table S2** and **Table S3** in the SM. These tables provide an overall understanding of the atomic composition of the materials. As an illustrative example, **Figure 1** shows the XPS spectra and peak deconvolution for C 1s, N 1s and O 1s regions of the sample N8THC900-2. **Figure 1A** shows the C 1s spectrum and the corresponding peak deconvolution. The main peak observed at 284.4 eV, $Csp^2$, corresponds to graphitic carbon, indicating the presence of carbon atoms arranged in a planar hexagonal lattice structure. Additionally, a series of peaks associated with N or O bonding can be identified. These include the $C_D$ peak at 283.5 eV, which is associated with defects in five-atom rings and/or to the formation of graphitic carbon nitrides. The C2 peak at 285.5 eV is assigned to carbon atoms outside the basal planes, exhibiting $sp^3$ hybridization. The C3 peak at 286.4 eV is assigned to ether- or hydroxyl-bonded C, or to C-bonded nitrogen oxides. The C4 peak at 287.6 eV indicates the presence of lactones or pyridines. The C5 peak at 289.2 eV is assigned to carboxylic acids, while the $C\pi$-$\pi^*$ peak at 291 eV is assigned to HUMO-LUMO transitions associated with the $Csp^2$ peak.

On the other hand, **Figure 1B** shows the XPS spectra in the N 1s region with the corresponding peak deconvolution. In the case of the non-doped carbons, the signals of the N 1s spectrum were too faint for reliable deconvolution and related analysis. Both N-doped series showed pyridinic species with the N6 peak at 398.3 eV as the main contribution, followed by the N5 peak at 400.2 eV, associated with pyrroles and/or pyridones. These two nitrogen functionalities are located on the edge of the carbon layers and are generally associated with an increase in the capacitance of N-doped carbon materials due to redox reactions, particularly in acidic electrolytes [44,45]. The N8THC series exhibited an increase in N6 species over N5 species for higher BOs, which is consistent with data reported in the literature [46,47]. However, it is important to note that this trend is also somewhat observed for the N4THC series. The presence of graphitic N, with the NQ peak at 401.2 eV, accounts for approximately 26 – 34 % in the N4THC series and 26 – 32 % in the N8THC series. The presence of this nitrogen functionality is highly desired, as it improves the electronic structure of the carbon material by reducing the band gap [45]. Finally, a peak at 402.9 eV corresponding to oxygen-bound nitrogen, N=O, represents approximately 9 – 15 % in both cases, without significant variations as the BO increases.

**Figure 1C** shows the deconvolution of the O 1s spectrum, revealing five distinct peaks. Among these, the quinone groups, with peak O1 at 530.9 eV, are the main ones, accounting for around 60 %. This observation corresponds to the characteristic catechol B-ring on the pine tannin precursor [48,49]. A smaller proportion of phenol/ether groups, with peak O2 at 532.3 eV, representing around 20 %, can be observed. Carboxylic acid groups, with peak O3 at 533.1 eV, accounting around 10 %, are also present. Additionally, a minor percentage of nitrogen-bound oxides, with peak O=N at 534.1 eV, and a small peak at 534.9 eV associated with chemisorbed water, can be observed. The main difference between the materials series is a slight increase in carboxylic acid groups (O3) at the expense of quinone-like groups (O1) for both N4THCs and N8THCs compared with THCs. This change is attributed to the tannin amination [20,26]. However, as depicted in **Figures 1E** and **1F**, the atomic contributions of specific N- and O-containing functional groups between the two N-doped series do not exhibit significant variations with BO.

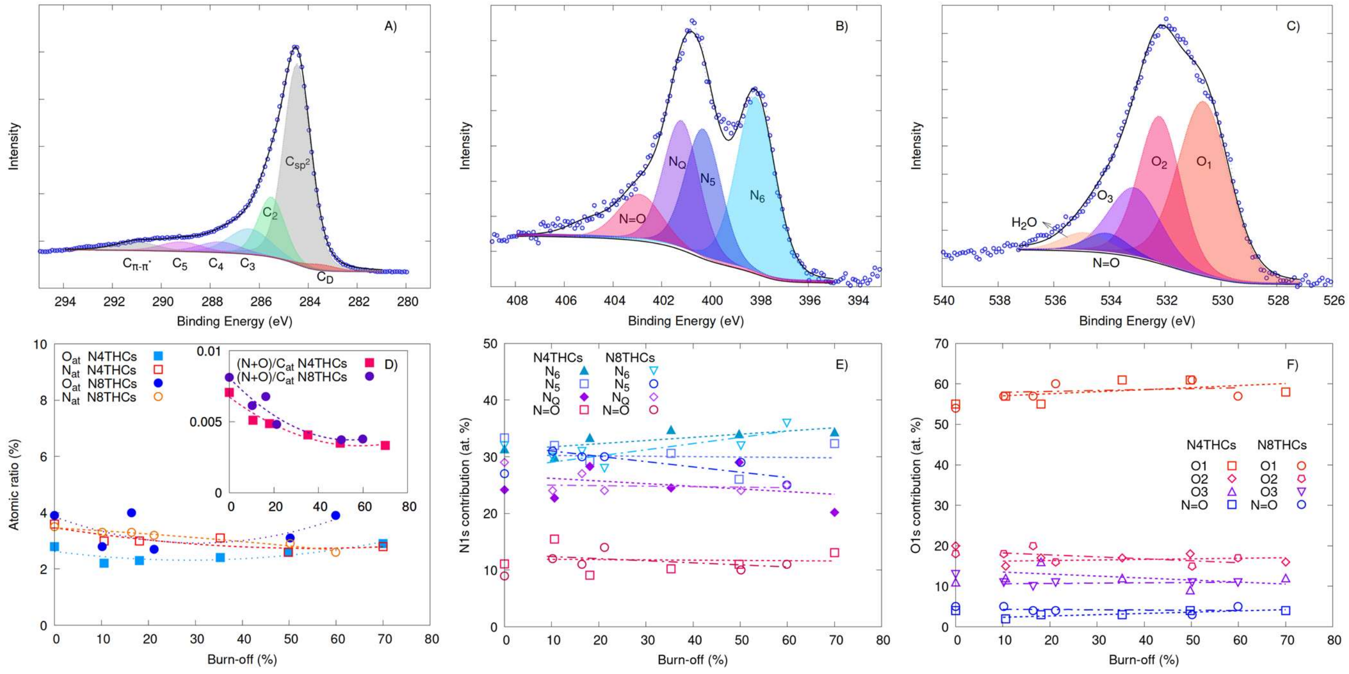

**Figure 1.** XPS spectra and deconvolution of the C 1s, N 1s and O 1s regions for sample N8THC900-2: A) C 1s; B) N 1s; C) O 1s. D) N and O atomic ratios estimated by XPS (inset: N+O/C ratios); E)

contribution of N functionalities according to N 1s region deconvolution; and F) contribution of O functionalities according to O 1s region deconvolution for N4THC (dashed trend line) and N8THC series (dotted-dashed trend line).

The role of oxygen functionalities on the capacitive performance of carbon materials has been extensively studied [50–52]. These functionalities play a crucial role as they improve the wettability of the materials and induce Faradaic contributions through electron transfer. However, it should be noted that the presence of oxygen functionalities leads to a decrease in surface electrical conductivity [51]. Existing literature suggests that quinone groups (referred to as O1) could be of crucial importance in high-energy density capacitors. Quinones are electrochemically active thanks to reversible two-electron and proton-coupled electron transfers with hydronium ions, especially in acidic solutions, which increase Faradaic contributions [22,50,53]. Besides, quinones allow the potential window to be widened, exhibit good chemical stability, and have no negative impact on electrode cycling stability [53]. Furthermore, as suggested by previous studies [21,27], it is anticipated that there will be a change in the surface chemistry of carbon materials due to the incorporation of nitrogen into the carbon matrix during the HTC step involving ammonia. It is worth noting that no significant differences in nitrogen to carbon (N/C) and oxygen to carbon (O/C) atomic ratios were observed with ammonia concentration or physical activation conditions as the BO increased (**Figure 1D**). However, the inset in **Figure 1D** shows that the $[(N+O)/C_{at}]$ ratio decreased slightly with increasing BO.

### 3.2. Textural properties and morphology

The TEM images in **Figure S2** (SM) provide a visual insight into the morphological changes induced by the use of aqueous ammonia in HTC. The composition of images includes the non-doped carbon material, called THC, alongside the two N-doped carbon materials, designated N4THC and

N8THC, presented in the previous section. THC consists of spherical particles of approximately 500 nm in diameter. These findings are consistent with those from hydrothermal carbonization, particularly for tannins, as reported by Braghiroli et al. [54], where spherical particles ranging from 200 nm to 5 µm were observed. In contrast, both N4THC and N8THC exhibit smaller and more cohesive spherical particles, approximately 50 nm in diameter. The TEM images in the section below illustrate materials subjected to carbonization at 800 °C under $N_2$ flow. A comparison reveals that carbonization induces the development of porosity without significantly altering the overall morphology of any of the materials studied. This can be seen by comparing TEM images from **Figure S2 A** and **Figure S2 D** (SM). Despite the carbonization process, the original spherical shape and structural integrity of the materials persist, highlighting the increase in porosity without compromising the fundamental morphological features [55,56].

$N_2$ adsorption-desorption isotherms are shown in **Figure 2**. All materials showed a combination of type I and type II isotherms. High $N_2$ uptake at very low $P/P°$ indicates the presence of significant microporosity [31], and as the activation time increased, $N_2$ adsorption also increased and the knee of the isotherms gradually broadened, indicating a widening of the micropores [31,57]. Additionally, a sharp increase in $N_2$ uptake near $P/P° = 0.97$ is observed, indicating the presence of large mesopores or condensation in interparticle voids [57]. However, significant differences can be observed in the $N_2$ isotherms across the various materials. In particular, those for non-doped carbons (**Figure S3A**, SM) showed a type H4 hysteresis loop, which closes near $P/P° = 0.5$. In contrast, those for carbons derived from N4THC (**Figure S3B**, SM) displayed an H3-type loop, which is often associated with capillary condensation [57]. Interestingly, the $N_2$ isotherms of the N8THC series (**Figure S3C**, SM) showed no noticeable loop. The $H_2$ adsorption isotherms of non-activated and $CO_2$-activated carbons can be found in **Figure S4** (SM), and for further details, the textural parameters estimated from the $N_2$ and $H_2$ isotherms at -196 °C are reported in **Table S4** in SM. The $A_{BET}$ is presented solely for comparison with other studies in the literature, given the well-known limitations of the BET method [58].

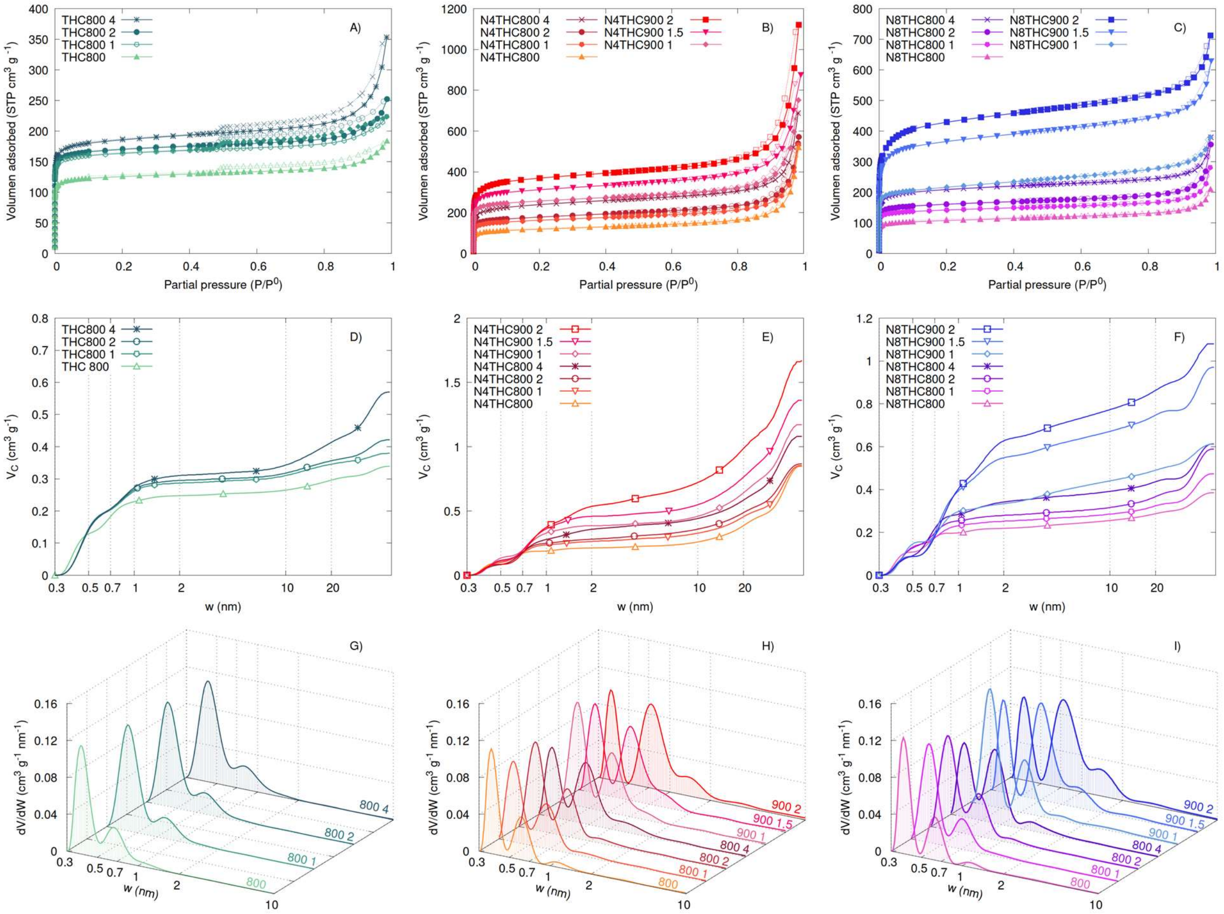

**Figure 2**. A, B, C) $N_2$ adsorption (solid symbols) – desorption (empty symbols) isotherms at -196 °C; D, E, F) cumulative; and G, H, I) differential volume pore size distributions (PSDs) estimated by 2D-NLDFT-HS: THC series (A, D, G), N4THC series (B, E, H), and N8THC series (C, F, and I).

As can be observed in **Figure 2G**, **2H** and **2I**, all carbon materials have a similar pore size distribution (PSD) with peaks centered on ultra-micropores, which is a characteristic feature of tannin-derived carbon materials [19,20,42]. For instance, two main peaks are observed on all the materials, one at ca.

0.4 nm and another of much less intensity at ca. 0.7 nm. For both N4THC and N8THC series, as activation conditions become more severe, a broadening of the ultra-micropores occurs, leading to a widening of the aforementioned peaks. The appearance of a third broad peak between 1 and 2 nm is observed under the most severe activation conditions (**Figure 2H** and **2I**). It should be noted that, although slightly, this third peak between 1 and 2 nm is also observed for non-activated N-doped samples (N4THC800 and N8THC800), suggesting that N could be responsible for promoting the formation of larger micropores.

The ultra-micropore volume followed a negative parabolic curve as the BO increase, as can be observed in **Figure 3A.4**, which is a well-documented behavior for ultra-micropores [29,59]. In addition, **Figure 3A.3** shows the monotonic increase of the supermicropore volume ($V_{s\mu}$) as a function of SSA for both N-doped series, with $V_{s\mu}$ increasing to 0.36 $cm^3$ $g^{-1}$ for N4THC900-2 and 0.43 $cm^3$ $g^{-1}$ for N8THC900-2. Mesopores are widely distributed throughout their range of pore sizes, without significant peaks, but they represent a significant fraction of the total pore volume on both N-doped carbon materials series, as is observed in **Figure 3B**. To clarify the differences between the N4THC and N8THC series, the mesopores region was divided into two zones, namely the range of wide mesopores, $10 < w < 50$ nm, and the range of narrow mesopores, $2 < w < 10$ nm, as observed in **Figure 3A.1** and **A.2**, respectively. The samples from the N4THC series have a substantial volume increase in the range of wide mesopores, increasing with SSA from ca. 0.64 $cm^3$ $g^{-1}$ (N4THC800) to a maximum of 1.19 $cm^3$ $g^{-1}$ (N4THC900-2). However, in the range of narrow mesopores (**Figure 3A.2**), the increase in volume is slightly noticeable. In contrast, the mesopore volume for the N8THC series changes significantly in the range of narrow mesopores, from 0.04 to 0.14 $cm^3g^{-1}$, while for wider mesopores it increases from 0.13 to 0.31 $cm^3$ $g^{-1}$. Although the reasons for these differences in porosity development are not evident, they are crucial in explaining the contrasting electrochemical behavior of the two series, as discussed in the next section.

Finally, **Figure 3C** shows the influence of BO on specific surface area (SSA), revealing a linear relationship between BO and SSA. The non-activated materials exhibited relatively low SSA values, with 990, 905, and 910 m$^2$ g$^{-1}$ for THC800, N4THC800 and N8THC800, respectively. As the BO increased due to the intensification of activation conditions, the SSA followed the same trend. For instance, N4THC900-2 and N8THC900-2, activated at 900 °C for 2 hours, reached values of 1710 and 1720 m$^2$g$^{-1}$, respectively, corresponding to a BO of ca. 70 % and 60 %, respectively.

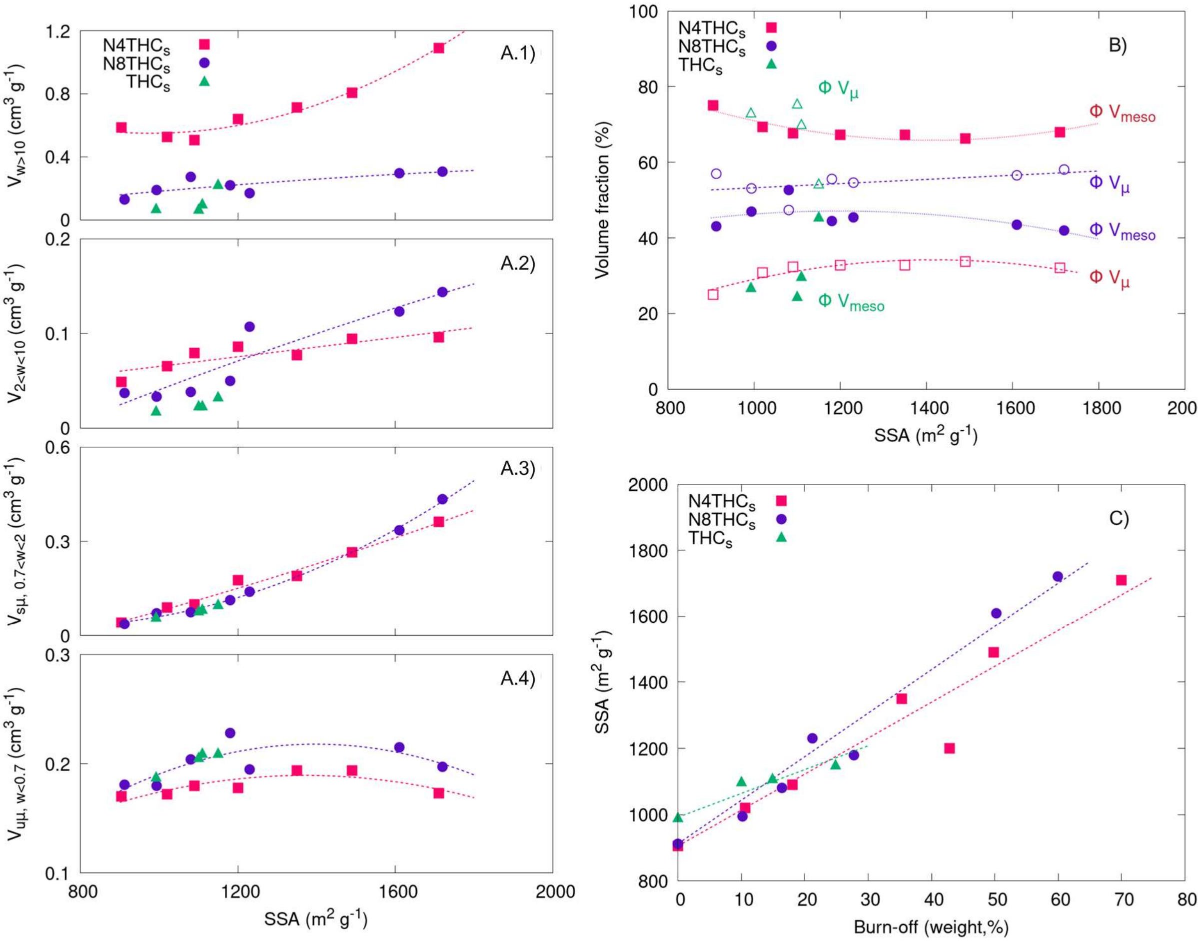

**Figure 3.** Volumes of: A.1) wide mesopores (10 < *w* < 50 nm); A.2) narrow mesopores (2 < *w* < 10 nm); A.3) supermicropores ($V_{sμ}$, 0.7 < *w* < 2 nm); and A.4) ultramicropores ($V_{uμ}$, *w* < 0.7 nm) as a

function of SSA. B) Volume fractions of micropores and mesopores ($\Phi\ V_{\mu}$ and $\Phi\ V_{\text{meso}}$, respectively) as a function of SSA. C) SSA as a function of burn-off (BO).

### 3.3. Electrochemical performance

Electrochemical impedance spectroscopy (EIS) was used as a technique to evaluate the kinetic and mass transport performance of the carbon materials as electrodes for ECs using 1 M $H_2SO_4$ as electrolyte. **Figure 4A** and **4B** show the Nyquist plot obtained in the two-electrode cell system for representative samples, while the Nyquist and Bode plots for all the materials are shown in **Figure S5** (SM). It can be seen that the graph did not start at the origin, but with a shift close to 1.8 Ω $cm^2$ along the $Z_r$ axis, associated with the bulk electrolyte resistance ($R_s$) [60]. Notable differences can be observed between samples, with the behavior of non-doped carbon materials being particularly evident. Taking THC800-4 as example for undoped materials, it is characterized by a significant charge transfer resistance ($R_{CT}$) indicated by a distinct semicircular area. In addition, the sample presented a semi-infinite Warburg impedance behavior in the region of mass transfer control, evidenced by the slope close to 45° at high values of $Z_r$ (**Figure 4B**), which indicates a high resistance to ion diffusion from the bulk to the surface of this material, with a non-capacitance behavior. The subpar electrochemical performance of undoped materials can be attributed to their surface chemistry, characterized by a significant presence of carboxylic acid species, as revealed by the XPS results in **Table S3** (SM). These carboxylic acid species have been demonstrated to hinder the formation of the electric double layer, thereby limiting electrical storage [61,62].

In contrast, the N-doped carbon materials exhibited a finite-space Warburg impedance, characterized by a straight line at high frequencies and a phase angle close to 90°, as shown the Bode plot in **Figure 4C**, which is typical of capacitive systems. Furthermore, the equivalent series resistance (ESR) can serve as a global parameter for comparing materials. For instance, THC800-4 had an ESR value of approximately 251.5 $\Omega$ $cm^{-2}$, which is almost two orders of magnitude higher than values estimated for N-doped carbon materials. The materials not submitted to physical activation, N4THC800 and N8THC800, had similar ESR values of ca. 11.4 and ca. 10.0 $\Omega$ $cm^{-2}$. It is worth noting that, in both cases, around 68 % and 63 % of the ESR values could be attributed to the $R_{CT}$, after subtracting the electrolyte resistance value ($R_S$) to calculate the respective percentages. In this context, the physical activation process resulted in a decrease in materials electrical resistivity by improving charge transfer, as evidenced by the significant reduction in the arc size shown in **Figure 4A**. For instance, N4THC900-2 and N8THC900-2, which underwent the most severe activation conditions in their respective series, had an ESR of ca. 4.2 and 3.8 $\Omega$ $cm^{-2}$, respectively, with $R_{CT}$ accounting for only 37 % and 45 % of the total ESR. The overall reduction in ESR of N-doped carbon materials can be attributed to carbon surface modifications resulting from tannin amination, which improves water affinity, as discussed above. In addition, pore widening and improved pore connectivity, attributed to the higher degree of activation [29], contributed to a better charge transfer process but also to better mass transfer (ion diffusion), as evidenced by the absence of Warburg impedance for N-doped and activated samples.

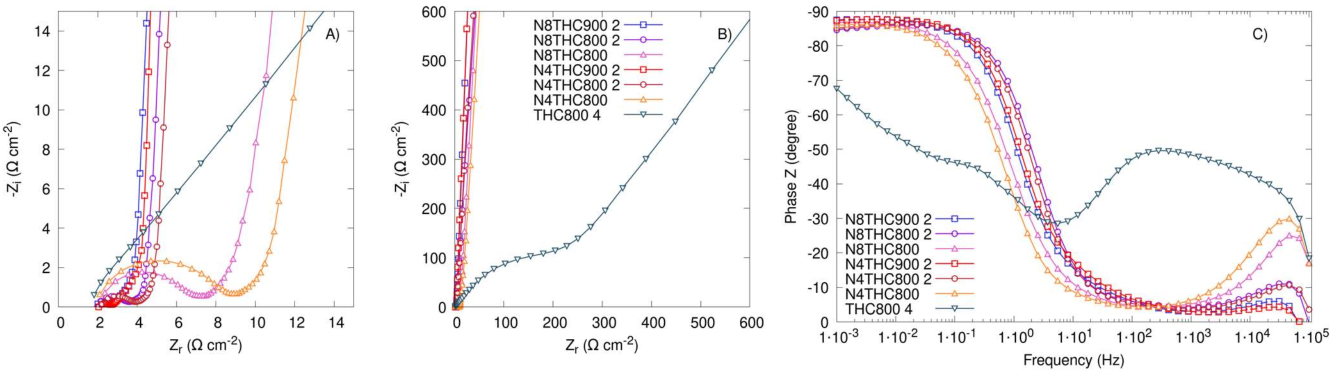

**Figure 4.** EIS results for representative N-doped and non-doped samples. For comparison purposes, THC800-4 is selected as the reference: A) Nyquist plot; B) large-scale Nyquist plot; C) Bode plot.

Cyclic voltammetry (CV) was conducted at scan rates from 5 mV s$^{-1}$ to 1 V s$^{-1}$, using a potential window of 0 – 1 V, which was chosen because of the use of an aqueous electrolyte. The results are presented in **Figure 5**, and further information is provided in **Figure S6** (SM). The non-doped carbon materials, as observed in the voltammograms of THC800-4 shown in **Figure S6A** (SM), did not exhibit capacitive behavior, even at low scan rates. However, the amination process improved the electro-chemical performance of the tannin-derived carbon materials (**Figures S6B** and **S6C**), in line with the EIS results discussed above. **Figure 5A** and **5B** show CV curves for representative carbon materials from the N4THC and N8THC series, respectively. A quasi-rectangular shape at a scan rate of 5 mV·s$^{-1}$ is observed on both cases, indicating near-ideal capacitive behavior. As the scan rate increased, the curves changed shape due to the gradual decrease in Faradaic contributions, so that the current aroused mainly from the formation of the electric double layer. In fact, at 5 mV·s$^{-1}$ the specific cell capacitance based on carbon material ($C_{\mathrm{CV,cell}}$), for N4THC800 and N8THC800 was approximately 37 F·g$^{-1}$ and 34 F·g$^{-1}$ (the electrode capacitance, also based on carbon material, $C_{\mathrm{CV,el}}$ is 148 F·g$^{-1}$ and 136 F·g$^{-1}$), respectively, with 43 % and 50 % retention, respectively, when tested at 1 V·s$^{-1}$. The activation process improved $C_{\mathrm{CV,cell}}$ values at low scan rates, with N4THC900-2 and N8THC900-2 exhibiting capacitance values of 43 F·g$^{-1}$ ($C_{CV,el}$ = 172 F·g$^{-1}$) and 51 F·g$^{-1}$ ($C_{CV,el}$ = 204 F·g$^{-1}$), respectively, at 5 mV·s$^{-1}$. Additionally, the capacitance retention reached remarkable values close to 65 % for both series when tested at a high scan rate of 1 V·s$^{-1}$.

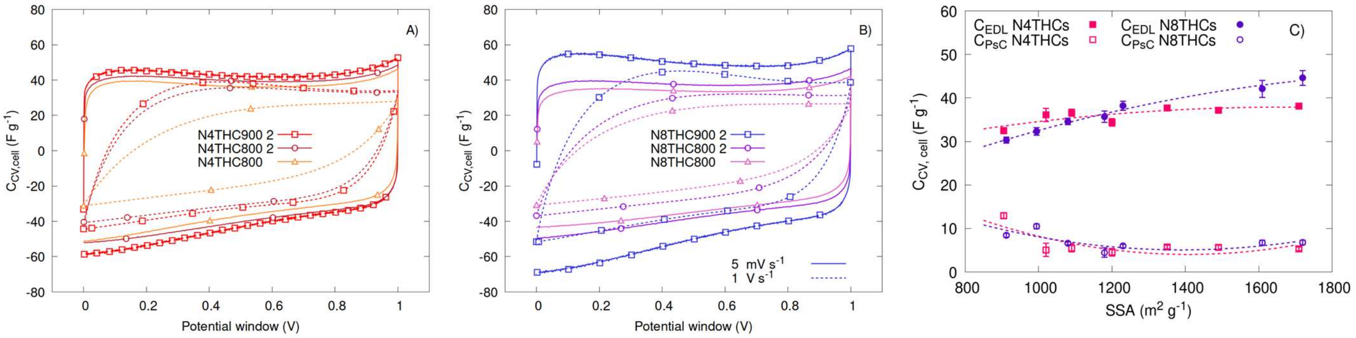

**Figure 5.** Cell capacitance ($C_{CV,cell}$) obtained by cyclic voltammetry at scan rates of 5 mV·s$^{-1}$ (solid line) and 1 V·s$^{-1}$ (dashed line) for: A) N4THC-; and B) N8THC-derived carbons. C) Electric double layer capacitance ($C_{EDL}$) and pseudocapacitance ($C_{PsC}$) estimated by Trassatti's method for the two series of N-doped carbon materials.

However, despite the relatively similar behavior in capacitance resulting from the activation process, there are still interesting features worth highlighting. In this context, Trassatti's method [38] was used to differentiate the double-layer capacitance ($C_{EDL}$) from the Faradaic contribution commonly referred to as pseudocapacitance ($C_{PsC}$). The dependence of the capacitance on the square root of the scan rate and its inverse ($v^{1/2}$ and $v^{-1/2}$, respectively) for the whole series is shown in **Figure S7** (SM), and a brief explanation of Trassatti's method is given in the SM, with the main results plotted in **Figure 5C** as a function of SSA. The pseudocapacitance arises from surface functionalities present in the material, which can improve mass or charge transfer [63]. It can be noticed that $C_{PsC}$ has comparable values for both series, displaying a similar downward trend, followed by a stabilization of its contribution. This behavior is a consequence of the chemical evolution of the carbon surface, as discussed previously (**Figure 1D**).

When considering $C_{\mathrm{EDL}}$, which originates from the textural properties of the carbon materials [64], it is essential to analyze the differences between the two series. Despite the noticeable increase in surface area for the N4THC series, from 905 $m^2$ $g^{-1}$ to 1710 $m^2$ $g^{-1}$ (see again **Table S4**, SM) for the most severe activation conditions, only a marginal enhancement in $C_{\mathrm{EDL}}$ was observed. This suggests a saturation of the surface, resulting in a slight increase in $C_{\mathrm{EDL}}$ from 32 to 38 F $g^{-1}$. In contrast, the N8THC series, although having similar values of surface area, exhibited a significant increase in $C_{\mathrm{EDL}}$ from 30 to 45 F $g^{-1}$. To understand this discrepancy between $C_{\mathrm{EDL}}$ trends for the N4THC and N8THC series, it is necessary to refer to the results shown in **Figure 2** and **Figure 3**. The PSD for both N-doped series, as can be seen in **Figures 2H** and **2I,** is similar in the micropore range, which is assumed the key to ion adsorption and efficient double-layer formation. However, although this has been extensively demonstrated [8,64–66], the influence of mesopores is often overlooked. Comparing the data in **Figure 3A**, it becomes clear that, at least for the electrolyte used in this study, the $C_{\mathrm{EDL}}$ improvement of N8THCs may be attributed to the development of narrow mesopores. In contrast, the N4THC series showed no significant development of mesopores in this size range.

Similar trends are observed in galvanostatic charge-discharge (GCD) tests performed by varying the applied specific current from 0.5 to 40 A $g^{-1}$. **Figure S8** (SM) shows the original charge-discharge curves within the 0 – 1 V potential window and at a specific current of 5 A $g^{-1}$, while **Figure 6A** shows the calculated specific cell capacitance obtained from the corresponding discharge curves ($C_{\mathrm{GCD,cell}}$). Remarkably, all curves, even at high specific current values, exhibited a triangular shape indicating capacitive behavior with a low potential drop (*iR*). At a specific current of 0.5 A $g^{-1}$, $C_{\mathrm{GCD,cell}}$ increased from 36 $F \cdot g^{-1}$ ($C_{\mathrm{GCD,el}}$= 144 $F \cdot g^{-1}$) for N4THC800 to 45 $F \cdot g^{-1}$ ($C_{\mathrm{GCD,el}}$= 180 $F \cdot g^{-1}$) for N4THC900-2.

As with the CV results, a significant increase in capacitance could be observed for the N8THC series compared with the N4THC series. Indeed, for the N8THC series, $C_{\mathrm{GCD,cell}}$ ranged from 32 $\mathrm{F{\cdot}g^{-1}}$ ($C_{\mathrm{GCD,el}}$= 128 $\mathrm{F{\cdot}g^{-1}}$) to 53 $\mathrm{F{\cdot}g^{-1}}$ ($C_{\mathrm{GCD,el}}$= 212 $\mathrm{F{\cdot}g^{-1}}$) for the same activation conditions. Interestingly, as discussed above, there were no notable differences in N or O contents between the two series (**Table S1**, SM) or in the proportions of surface functionalities (**Figure 1E** and **Figure 1F**). Therefore, the observed increase in $C_{\mathrm{GCD,cell}}$ could, once again, be attributed to the development of narrow mesopores. It is worth noting that while the capacitance values obtained by GCD, at low specific current, and CV, at low scan rate, were comparable, the $C_{\mathrm{GCD,cell}}$ retention was higher than that obtained from CV tests. For instance, N4THC900-2 and N8THC900-2, the best performing materials in their respective series, demonstrated impressive retention rates in GCD tests. At a specific current of 5 A $\mathrm{g^{-1}}$, N4THC900-2 retained 82 % of its initial capacitance, while N8THC900-2 retained 81 %. Even at a higher specific current of 40 A $\mathrm{g^{-1}}$, both materials maintained a high level of stability, with N4THC900-2 retaining 72 % of its initial capacitance and N8THC900-2 retaining 71 %. Therefore, to assess their cycling stability, N4THC900-2 and N8THC900-2 were subjected to 30,000 continuous GCD cycles at a specific current of 5 A $\mathrm{g^{-1}}$. **Figure 6B** depicts the cycling stability of both carbon materials, demonstrating a remarkable retention of ca. 96 % for N4THC900-2 and N8THC900-2 relative to their initial capacitance.

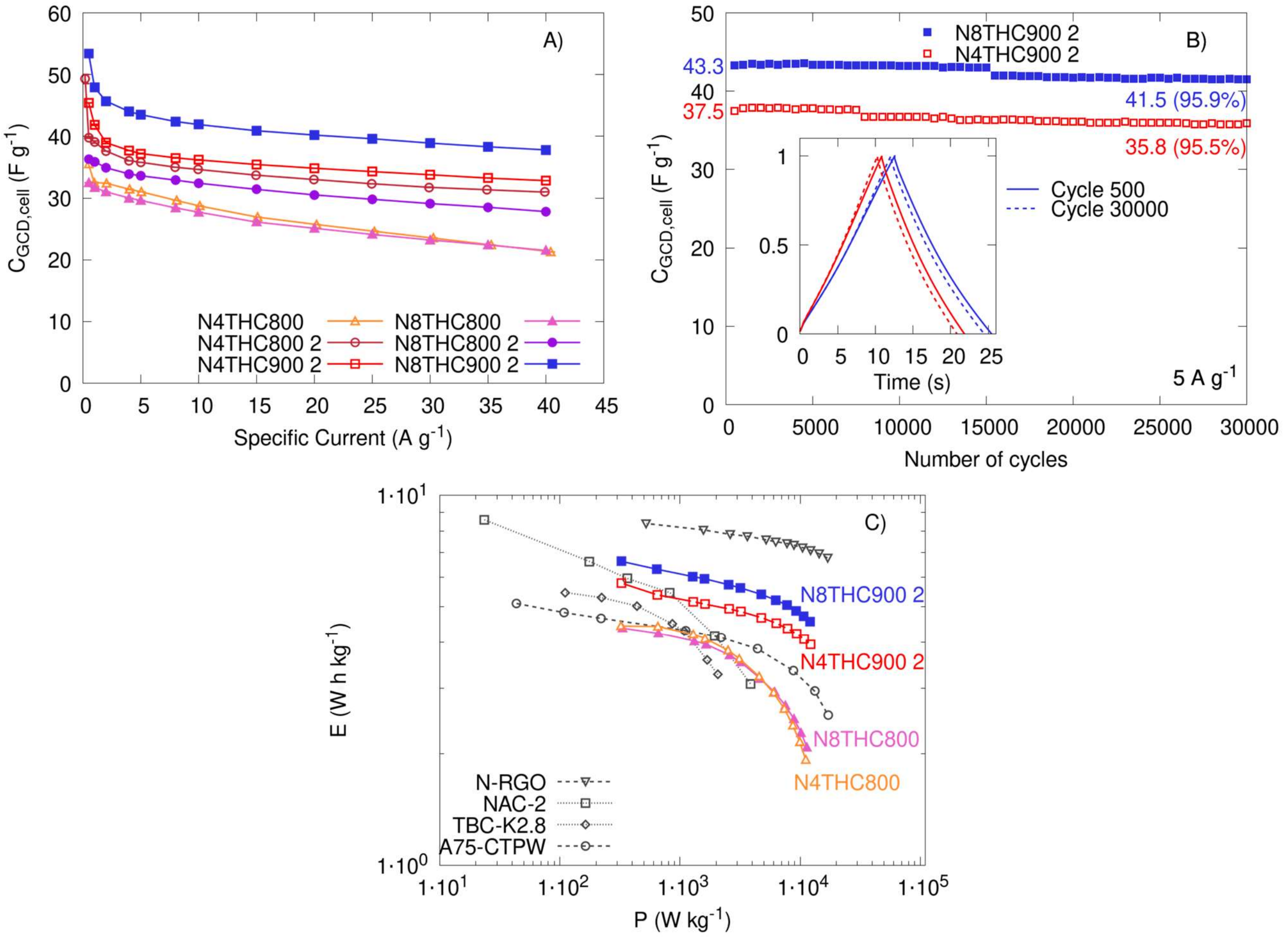

**Figure 6**. A) Specific cell capacitances calculated from GCD curves ($C_{\mathrm{GCD,cell}}$) for N4THC and N8THC series; B) cycling stability of N8THC900-2 and N4THC900-2 at 5 A g$^{-1}$, the inset corresponding to GCD curves for cycle #500 (solid line) and cycle #30,000 (dashed line); C) Ragone plot calculated from GCD measurements from 2 to 40 A g$^{-1}$ and comparison with the literature (N-RGO [44], NAC-2 [67], TBC-K2.8 [19], A75-CTPW [9]).

The inset in **Figure 6B** reveals that the triangular-shaped charge-discharge curve remained largely unchanged after the cycling test, indicating the excellent stability of the surface functionalities of these materials. It is worth noting that although pseudocapacitive contributions represented approximately 10 % of the total capacitance, as suggested by the CV results discussed earlier (**Figure 5C**), they had no significantly impact on the stability of the materials.

The Ragone plot in **Figure 6C** shows the electrochemical performance of N4THC900-2 and N8THC900-2. For comparison purposes, this figure also includes electrochemical characterization data for other N-doped and tannin-derived carbons reported in the open literature [9,44,67,68]. As anticipated from the previous results, the material exhibiting the best performance was N8THC900-2, with a specific energy of approximately 6.6 $W \cdot h \cdot kg^{-1}$ at a specific power of around 3240 $W \cdot kg^{-1}$ The specific energy gradually decreased as the specific power increased, reaching approximately 4.6 $W \cdot h \cdot kg^{-1}$ at about 12100 $W \cdot kg^{-1}$. Although the specific energy of these ACs cannot exceed that obtained with N-doped reduced graphene oxide (N-RGO, $A_{BET}$ = 355 $m^2$ $g^{-1}$, $O_{XPS}$ = 12.6 at. %, $N_{XPS}$ = 3.0 at. %) [44], it is noteworthy that they outperformed other N-doped ACs [67,68], especially at high rates. Similarly, an improvement in the electrochemical performance of N8THC900-2 (SSA = 1720 $m^2$ $g^{-1}$, $O_{XPS}$ = 2.6 at %, $N_{XPS}$ = 3.9 at. %) was observed compared to previously reported non-doped tannin-derived ACs obtained by $CO_2$ activation (SSA = 1614 $m^2$ $g^{-1}$, $O_{XPS}$ = 5.0 at.%) [9] and by KOH activation (TBC-K2.8: SSA = 2190 $m^2$ $g^{-1}$, $O_{XPS}$ = 7.5 at.%) [19], all tested under similar conditions, confirming the benefits of N-doping in enhancing the electrochemical performance of materials.

## Conclusion

This study shows that nitrogen doping by hydrohermal carbonization in ammonia not only changed the surface chemistry of the resulting carbon materials but also improved their textural properties after $CO_2$ activation. These changes enhanced the electrochemical performance of the N-doped activated carbons (ACs) when used as supercapacitor electrodes. The concentration of ammonia used had no significant impact on the N content nor the nature of the surface chemistry of the carbon materials. However, it did affect the development of textural properties during $CO_2$ activation, with a greater effect observed at higher ammonia concentration. The best-performing material achieved a specific electrode capacitance value, based on carbon material, of 212 F $g^{-1}$ at 0.5 A $g^{-1}$ and a capacitance retention of 71 % at 40 A $g^{-1}$. It also demonstrated outstanding cycling stability with capacitance retention of ca. 96 % after 30,000 cycles. These N-doped ACs outperformed similar carbon materials, particularly at high output power, demonstrating that N-doped ACs derived from tannins are suitable electrode materials for electrochemical capacitors, especially when high-rate performance and remarkable electrochemical stability are required.

## Acknowledgments

O. Pinto-Burgos thanks ANID - Subdirección de Capital Humano/Doctorado, # 2019/21190633. V. Fierro, A. Celzard, and J. Castro-Gutiérrez acknowledge the financial support of the European Regional Development Fund (ERDF) through the TALiSMAN and TALiSMAN2 projects. P.S. Poon and J. Matos thank ANID-FONDEF project 19I10003 and ANID-FONDECYT project 1220228. J. Matos also thanks ANID-ANILLO project ATE220014.

## Declaration of competing interest

The authors declare that they have no known competing financial interests or personal relationships that could have appeared to influence the work reported in this paper.

## Authors' contributions

**O. Pinto-Burgos** contributed to synthesis, characterization, textural and electrochemical testing, analysis, writing and revision. **J. Castro-Gutierrez** contributed to characterization, analysis, data curation and revision. **P.S. Poon** contributed to synthesis and editing. **M.T. Izquierdo** contributed to XPS characterization. **A. Celzard** contributed to analysis, data curation and editing. **V. Fierro** and **J. Matos** contributed to conceptualization, data curation, analysis, writing and revision.

# References

[1] P. Simon, Y. Gogotsi, Perspectives for electrochemical capacitors and related devices, Nat. Mater. 19 (2020) 1151–1163. https://doi.org/10.1038/s41563-020-0747-z.

[2] T.M. Gür, Review of electrical energy storage technologies, materials and systems: challenges and prospects for large-scale grid storage, Energy Environ. Sci. 11 (2018) 2696–2767. https://doi.org/10.1039/C8EE01419A.

[3] M. Horn, J. MacLeod, M. Liu, J. Webb, N. Motta, Supercapacitors: A new source of power for electric cars?, Economic Analysis and Policy 61 (2019) 93–103. https://doi.org/10.1016/j.eap.2018.08.003.

[4] A. Burke, Ultracapacitors: why, how, and where is the technology, Journal of Power Sources 91 (2000) 37–50. https://doi.org/10.1016/S0378-7753(00)00485-7.

[5] B.K. Kim, S. Sy, A. Yu, J. Zhang, Electrochemical Supercapacitors for Energy Storage and Conversion, in: J. Yan (Ed.), Handbook of Clean Energy Systems, John Wiley & Sons, Ltd, Chichester, UK, 2015: pp. 1–25. https://doi.org/10.1002/9781118991978.hces112.

[6] Z. Lin, E. Goikolea, A. Balducci, K. Naoi, P.L. Taberna, M. Salanne, G. Yushin, P. Simon, Materials for supercapacitors: When Li-ion battery power is not enough, Materials Today 21 (2018) 419–436. https://doi.org/10.1016/j.mattod.2018.01.035.

[7] E. Frackowiak, Q. Abbas, F. Béguin, Carbon/carbon supercapacitors, Journal of Energy Chemistry 22 (2013) 226–240. https://doi.org/10.1016/S2095-4956(13)60028-5.

[8] C. Largeot, C. Portet, J. Chmiola, P.-L. Taberna, Y. Gogotsi, P. Simon, Relation between the Ion Size and Pore Size for an Electric Double-Layer Capacitor, J. Am. Chem. Soc. 130 (2008) 2730–2731. https://doi.org/10.1021/ja7106178.

[9] J. Castro-Gutiérrez, N. Díez, M. Sevilla, M.T. Izquierdo, J. Ghanbaja, A. Celzard, V. Fierro, High-Rate Capability of Supercapacitors Based on Tannin-Derived Ordered Mesoporous Carbons, ACS Sustainable Chem. Eng. 7 (2019) 17627–17635. https://doi.org/10.1021/acssuschemeng.9b03407.

[10] F. Béguin, V. Presser, A. Balducci, E. Frackowiak, Carbons and Electrolytes for Advanced Supercapacitors, Advanced Materials 26 (2014) 2219–2251. https://doi.org/10.1002/adma.201304137.

[11] M. Zhong, Q.F. Tang, Z.G. Qiu, W.P. Wang, X.Y. Chen, Z.J. Zhang, A novel electrolyte of ternary deep eutectic solvent for wide temperature region supercapacitor with superior performance, Journal of Energy Storage 32 (2020) 101904. https://doi.org/10.1016/j.est.2020.101904.

[12] B.D. Assresahegn, T. Brousse, D. Bélanger, Advances on the use of diazonium chemistry for functionalization of materials used in energy storage systems, Carbon 92 (2015) 362–381. https://doi.org/10.1016/j.carbon.2015.05.030.

[13] S. Ghosh, S. Barg, S.M. Jeong, K. (Ken) Ostrikov, Heteroatom-Doped and Oxygen-Functionalized Nanocarbons for High-Performance Supercapacitors, Adv. Energy Mater. 10 (2020) 2001239. https://doi.org/10.1002/aenm.202001239.

[14] C.O. Ania, P.A. Armstrong, T.J. Bandosz, F. Beguin, A.P. Carvalho, A. Celzard, E. Frackowiak, M.A. Gilarranz, K. László, J. Matos, M.F.R. Pereira, Engaging nanoporous carbons in "beyond adsorption" applications: Characterization, challenges and performance, Carbon 164 (2020) 69–84. https://doi.org/10.1016/j.carbon.2020.03.056.

[15] J. Matos, V. Fierro, R. Montaña, E. Rivero, A.M. de Yuso, W. Zhao, A. Celzard, High surface area microporous carbons as photoreactors for the catalytic photodegradation of methylene blue under UV–vis irradiation, Applied Catalysis A: General 517 (2016) 1–11. https://doi.org/10.1016/j.apcata.2016.02.031.

[16] D. Momodu, M. Madito, F. Barzegar, A. Bello, A. Khaleed, O. Olaniyan, J. Dangbegnon, N. Manyala, Activated carbon derived from tree bark biomass with promising material properties for

supercapacitors, J Solid State Electrochem 21 (2017) 859–872. https://doi.org/10.1007/s10008-016-3432-z.

[17] W. Sun, S.M. Lipka, C. Swartz, D. Williams, F. Yang, Hemp-derived activated carbons for supercapacitors, Carbon 103 (2016) 181–192. https://doi.org/10.1016/j.carbon.2016.02.090.

[18] J.L. Gómez-Urbano, G. Moreno-Fernández, M. Arnaiz, J. Ajuria, T. Rojo, D. Carriazo, Graphene-coffee waste derived carbon composites as electrodes for optimized lithium ion capacitors, Carbon 162 (2020) 273–282. https://doi.org/10.1016/j.carbon.2020.02.052.

[19] S. Pérez-Rodríguez, O. Pinto, M.T. Izquierdo, C. Segura, P.S. Poon, A. Celzard, J. Matos, V. Fierro, Upgrading of pine tannin biochars as electrochemical capacitor electrodes, Journal of Colloid and Interface Science 601 (2021) 863–876. https://doi.org/10.1016/j.jcis.2021.05.162.

[20] A. Sanchez-Sanchez, M.T. Izquierdo, S. Mathieu, J. González-Álvarez, A. Celzard, V. Fierro, Outstanding electrochemical performance of highly N- and O-doped carbons derived from pine tannin, Green Chem. 19 (2017) 2653–2665. https://doi.org/10.1039/C7GC00491E.

[21] F.L. Braghiroli, V. Fierro, A. Szczurek, N. Stein, J. Parmentier, A. Celzard, Electrochemical performances of hydrothermal tannin-based carbons doped with nitrogen, Industrial Crops and Products 70 (2015) 332–340. https://doi.org/10.1016/j.indcrop.2015.03.046.

[22] J. Castro-Gutiérrez, A. Celzard, V. Fierro, Energy Storage in Supercapacitors: Focus on Tannin-Derived Carbon Electrodes, Front. Mater. 7 (2020) 217. https://doi.org/10.3389/fmats.2020.00217.

[23] J. Quílez-Bermejo, S. Pérez-Rodríguez, A. Celzard, V. Fierro, Progress in the Use of Biosourced Phenolic Molecules for Electrode Manufacturing, Front. Mater. 9 (2022) 810575. https://doi.org/10.3389/fmats.2022.810575.

[24] G. Tondi, V. Fierro, A. Pizzi, A. Celzard, Tannin-based carbon foams, Carbon 47 (2009) 1480–1492. https://doi.org/10.1016/j.carbon.2009.01.041.

[25] K. Hashida, R. Makino, S. Ohara, Amination of pyrogallol nucleus of condensed tannins and related polyphenols by ammonia water treatment, Hfsg 63 (2009) 319–326. https://doi.org/10.1515/HF.2009.043.

[26] F.L. Braghiroli, V. Fierro, M.T. Izquierdo, J. Parmentier, A. Pizzi, A. Celzard, Nitrogen-doped carbon materials produced from hydrothermally treated tannin, Carbon 50 (2012) 5411–5420. https://doi.org/10.1016/j.carbon.2012.07.027.

[27] A.G. Pandolfo, A.F. Hollenkamp, Carbon properties and their role in supercapacitors, Journal of Power Sources 157 (2006) 11–27. https://doi.org/10.1016/j.jpowsour.2006.02.065.

[28] J. Wang, S. Kaskel, KOH activation of carbon-based materials for energy storage, J. Mater. Chem. 22 (2012) 23710. https://doi.org/10.1039/c2jm34066f.

[29] J. Castro-Gutiérrez, R.L.S. Canevesi, M. Emo, M.T. Izquierdo, A. Celzard, V. Fierro, CO2 outperforms KOH as an activator for high-rate supercapacitors in aqueous electrolyte, Renewable and Sustainable Energy Reviews 167 (2022) 112716. https://doi.org/10.1016/j.rser.2022.112716.

[30] A. Berg, L. Olave, P. Navarrete, Process for obtaining low and medium molecular weight Polyphenols and standardized solid fuel from tree wood or bark, US20090077871A1, 2009. https://patents.google.com/patent/US20090077871A1/en?inventor=berg+alex&assignee=Berg+Alex (accessed November 14, 2022).

[31] M. Thommes, K. Kaneko, A.V. Neimark, J.P. Olivier, F. Rodriguez-Reinoso, J. Rouquerol, K.S.W. Sing, Physisorption of gases, with special reference to the evaluation of surface area and pore size distribution (IUPAC Technical Report), Pure and Applied Chemistry 87 (2015) 1051–1069. https://doi.org/10.1515/pac-2014-1117.

[32] J. Jagiello, J. Kenvin, C.O. Ania, J.B. Parra, A. Celzard, V. Fierro, Exploiting the adsorption of simple gases O2 and H2 with minimal quadrupole moments for the dual gas characterization of nanoporous carbons using 2D-NLDFT models, Carbon 160 (2020) 164–175. https://doi.org/10.1016/j.carbon.2020.01.013.

[33] L.S. Blankenship, J. Jagiello, R. Mokaya, Confirmation of pore formation mechanisms in biochars and activated carbons by dual isotherm analysis, Mater. Adv. 3 (2022) 3961–3971. https://doi.org/10.1039/D2MA00141A.

[34] M. Smith, L. Scudiero, J. Espinal, J.-S. McEwen, M. Garcia-Perez, Improving the deconvolution and interpretation of XPS spectra from chars by ab initio calculations, Carbon 110 (2016) 155–171. https://doi.org/10.1016/j.carbon.2016.09.012.

[35] M. Ayiania, M. Smith, A.J.R. Hensley, L. Scudiero, J.-S. McEwen, M. Garcia-Perez, Deconvoluting the XPS spectra for nitrogen-doped chars: An analysis from first principles, Carbon 162 (2020) 528–544. https://doi.org/10.1016/j.carbon.2020.02.065.

[36] A.J. Bard, L.R. Faulkner, Electrochemical Methods: Fundamentals and Applications, Wiley, 2000. https://books.google.cl/books?id=kv56QgAACAAJ.

[37] N.O. Laschuk, E.B. Easton, O.V. Zenkina, Reducing the resistance for the use of electrochemical impedance spectroscopy analysis in materials chemistry, RSC Adv. 11 (2021) 27925–27936. https://doi.org/10.1039/D1RA03785D.

[38] S. Ardizzone, G. Fregonara, S. Trasatti, “Inner” and “outer” active surface of RuO2 electrodes, Electrochimica Acta 35 (1990) 263–267. https://doi.org/10.1016/0013-4686(90)85068-X.

[39] M.D. Stoller, R.S. Ruoff, Best practice methods for determining an electrode material’s performance for ultracapacitors, Energy Environ. Sci. 3 (2010) 1294. https://doi.org/10.1039/c0ee00074d.

[40] A. Laheäär, P. Przygocki, Q. Abbas, F. Béguin, Appropriate methods for evaluating the efficiency and capacitive behavior of different types of supercapacitors, Electrochemistry Communications 60 (2015) 21–25. https://doi.org/10.1016/j.elecom.2015.07.022.

[41] A. Celzard, V. Fierro, “Green”, innovative, versatile and efficient carbon materials from polyphenolic plant extracts, Carbon 167 (2020) 792–815. https://doi.org/10.1016/j.carbon.2020.05.053.

[42] J. Castro-Gutiérrez, N. Díez, M. Sevilla, M.T. Izquierdo, A. Celzard, V. Fierro, Model carbon materials derived from tannin to assess the importance of pore connectivity in supercapacitors, Renewable and Sustainable Energy Reviews 151 (2021) 111600. https://doi.org/10.1016/j.rser.2021.111600.

[43] Y. Yamada, H. Tanaka, S. Kubo, S. Sato, Unveiling bonding states and roles of edges in nitrogen-doped graphene nanoribbon by X-ray photoelectron spectroscopy, Carbon 185 (2021) 342–367. https://doi.org/10.1016/j.carbon.2021.08.085.

[44] Y.-H. Lee, K.-H. Chang, C.-C. Hu, Differentiate the pseudocapacitance and double-layer capacitance contributions for nitrogen-doped reduced graphene oxide in acidic and alkaline electrolytes, Journal of Power Sources 227 (2013) 300–308. https://doi.org/10.1016/j.jpowsour.2012.11.026.

[45] G. Lota, K. Lota, E. Frackowiak, Nanotubes based composites rich in nitrogen for supercapacitor application, Electrochemistry Communications 9 (2007) 1828–1832. https://doi.org/10.1016/j.elecom.2007.04.015.

[46] J.R. Pels, F. Kapteijn, J.A. Moulijn, Q. Zhu, K.M. Thomas, Evolution of nitrogen functionalities in carbonaceous materials during pyrolysis, Carbon 33 (1995) 1641–1653. https://doi.org/10.1016/0008-6223(95)00154-6.

[47] J. Quílez-Bermejo, M. Melle-Franco, E. San-Fabián, E. Morallón, D. Cazorla-Amorós, Towards understanding the active sites for the ORR in N-doped carbon materials through fine-tuning of nitrogen functionalities: an experimental and computational approach, J. Mater. Chem. A 7 (2019) 24239–24250. https://doi.org/10.1039/C9TA07932G.

[48] C.S. Ku, S.P. Mun, Characterization of proanthocyanidin in hot water extract isolated from Pinus radiata bark, Wood Sci Technol 41 (2007) 235. https://doi.org/10.1007/s00226-006-0103-8.

[49] O. Pinto, R. Romero, M. Carrier, J. Appelt, C. Segura, Fast pyrolysis of tannins from pine bark as a renewable source of catechols, Journal of Analytical and Applied Pyrolysis 136 (2018) 69–76. https://doi.org/10.1016/j.jaap.2018.10.022.

[50] J.E. Zuliani, S. Tong, C.Q. Jia, D.W. Kirk, Contribution of surface oxygen groups to the measured capacitance of porous carbon supercapacitors, Journal of Power Sources 395 (2018) 271–279. https://doi.org/10.1016/j.jpowsour.2018.05.046.

[51] Y. He, Y. Zhang, X. Li, Z. Lv, X. Wang, Z. Liu, X. Huang, Capacitive mechanism of oxygen functional groups on carbon surface in supercapacitors, Electrochimica Acta 282 (2018) 618–625. https://doi.org/10.1016/j.electacta.2018.06.103.

[52] C.-T. Hsieh, H. Teng, Influence of oxygen treatment on electric double-layer capacitance of activated carbon fabrics, Carbon 40 (2002) 667–674. https://doi.org/10.1016/S0008-6223(01)00182-8.

[53] S.P. Ega, P. Srinivasan, Quinone materials for supercapacitor: Current status, approaches, and future directions, Journal of Energy Storage 47 (2022) 103700. https://doi.org/10.1016/j.est.2021.103700.

[54] F.L. Braghiroli, V. Fierro, M.T. Izquierdo, J. Parmentier, A. Pizzi, A. Celzard, Kinetics of the hydrothermal treatment of tannin for producing carbonaceous microspheres, Bioresource Technology 151 (2014) 271–277. https://doi.org/10.1016/j.biortech.2013.10.045.

[55] B. Hu, K. Wang, L. Wu, S. Yu, M. Antonietti, M. Titirici, Engineering Carbon Materials from the Hydrothermal Carbonization Process of Biomass, Advanced Materials 22 (2010) 813–828. https://doi.org/10.1002/adma.200902812.

[56] F. Braghiroli, V. Fierro, A. Szczurek, P. Gadonneix, J. Ghanbaja, J. Parmentier, G. Medjahdi, A. Celzard, Hydrothermal Treatment of Tannin: A Route to Porous Metal Oxides and Metal/Carbon Hybrid Materials, Inorganics 5 (2017) 7. https://doi.org/10.3390/inorganics5010007.

[57] F.J. Sotomayor, K.A. Cychosz, M. Thommes, Characterization of Micro/Mesoporous Materials by Physisorption: Concepts and Case Studies, (2018) 17.

[58] J. Rouquerol, P. Llewellyn, F. Rouquerol, Is the bet equation applicable to microporous adsorbents?, in: Studies in Surface Science and Catalysis, Elsevier, 2007: pp. 49–56. https://doi.org/10.1016/S0167-2991(07)80008-5.

[59] M.V. Navarro, N.A. Seaton, A.M. Mastral, R. Murillo, Analysis of the evolution of the pore size distribution and the pore network connectivity of a porous carbon during activation, Carbon 44 (2006) 2281–2288. https://doi.org/10.1016/j.carbon.2006.02.029.

[60] O. Gharbi, M.T.T. Tran, B. Tribollet, M. Turmine, V. Vivier, Revisiting cyclic voltammetry and electrochemical impedance spectroscopy analysis for capacitance measurements, Electrochimica Acta 343 (2020) 136109. https://doi.org/10.1016/j.electacta.2020.136109.

[61] H. Oda, A. Yamashita, S. Minoura, M. Okamoto, T. Morimoto, Modification of the oxygen-containing functional group on activated carbon fiber in electrodes of an electric double-layer capacitor, Journal of Power Sources 158 (2006) 1510–1516. https://doi.org/10.1016/j.jpowsour.2005.10.061.

[62] Y.-R. Nian, H. Teng, Influence of surface oxides on the impedance behavior of carbon-based electrochemical capacitors, Journal of Electroanalytical Chemistry 540 (2003) 119–127. https://doi.org/10.1016/S0022-0728(02)01299-8.

[63] M. Seredych, D. Hulicova-Jurcakova, G.Q. Lu, T.J. Bandosz, Surface functional groups of carbons and the effects of their chemical character, density and accessibility to ions on electrochemical performance, Carbon 46 (2008) 1475–1488. https://doi.org/10.1016/j.carbon.2008.06.027.

[64] E. Raymundo-Piñero, K. Kierzek, J. Machnikowski, F. Béguin, Relationship between the nanoporous texture of activated carbons and their capacitance properties in different electrolytes, Carbon 44 (2006) 2498–2507. https://doi.org/10.1016/j.carbon.2006.05.022.

[65] M. Liu, X. Yang, X. Wu, X. Wang, Y. Li, F. Ma, J. Zhou, Understanding the pore-structure dependence of supercapacitive performance for microporous carbon in aqueous KOH and H2SO4 electrolytes, Electrochimica Acta 401 (2022) 139422. https://doi.org/10.1016/j.electacta.2021.139422.

[66] J. Chmiola, G. Yushin, Y. Gogotsi, C. Portet, P. Simon, P.L. Taberna, Anomalous Increase in Carbon Capacitance at Pore Sizes Less Than 1 Nanometer, Science 313 (2006) 1760–1763. https://doi.org/10.1126/science.1132195.

[67] M.K. Sahoo, G.R. Rao, A high energy flexible symmetric supercapacitor fabricated using N-doped activated carbon derived from palm flowers, Nanoscale Adv. 3 (2021) 5417–5429. https://doi.org/10.1039/D1NA00261A.

[68] K. Lota, I. Acznik, A. Sierczynska, G. Lota, The capacitance properties of activated carbon obtained from chitosan as the electrode material for electrochemical capacitors, Materials Letters 173 (2016) 72–75. https://doi.org/10.1016/j.matlet.2016.03.031.

## Captions of Figures

**Figure 1.** XPS spectra and deconvolution of the C 1s, N 1s and O 1s regions for sample N8THC900-2: A) C 1s; B) N 1s; C) O 1s. D) N and O atomic ratios estimated by XPS (inset: N+O/C ratios); E) contribution of N functionalities according to N 1s region deconvolution; and F) contribution of O functionalities according to O 1s region deconvolution for N4THC (dashed trend line) and N8THC series (dotted-dashed trend line).

**Figure 2**. A, B, C) $N_2$ adsorption (solid symbols) – desorption (empty symbols) isotherms at -196 °C; D, E, F) cumulative; and G, H, I) differential volume pore size distributions (PSDs) estimated by 2D-NLDFT-HS: THC series (A, D, G), N4THC series (B, E, H), and N8THC series (C, F, and I).

**Figure 3.** Volumes of: A.1) wide mesopores ($10 < w < 50$ nm); A.2) narrow mesopores ($2 < w < 10$ nm); A.3) supermicropores ($V_{\mathrm{s\mu}}$, $0.7 < w < 2$ nm); and A.4) ultramicropores ($V_{\mathrm{u\mu}}$, $w < 0.7$ nm) as a function of SSA. B) Volume fractions of micropores and mesopores ($\Phi\ V_{\mu}$ and $\Phi\ V_{\mathrm{meso}}$, respectively) as a function of SSA. C) SSA as a function of burn-off (BO).

**Figure 4.** EIS results for representative N-doped and non-doped samples. For comparison purposes, THC800-4 is selected as the reference: A) Nyquist plot; B) large-scale Nyquist plot; C) Bode plot.

**Figure 5.** Cell capacitance ($C_{\mathrm{CV,cell}}$) obtained by cyclic voltammetry at scan rates of 5 $\mathrm{mV\cdot s^{-1}}$ (solid line) and 1 $\mathrm{V\cdot s^{-1}}$ (dashed line) for: A) N4THC-; and B) N8THC-derived carbons. C) Electric double layer capacitance ($C_{\mathrm{EDL}}$) and pseudocapacitance ($C_{\mathrm{PsC}}$) estimated by Trassatti's method for the two series of N-doped carbon materials.

**Figure 6**. A) Specific cell capacitances calculated from GCD curves ($C_{\mathrm{GCD,cell}}$) for N4THC and N8THC series; B) cycling stability of N8THC900-2 and N4THC900-2 at 5 A $\mathrm{g^{-1}}$, the inset correspond-

ing to GCD curves for cycle #500 (solid line) and cycle #30,000 (dashed line); C) Ragone plot calculated from GCD measurements from 2 to 40 A $g^{-1}$ and comparison with the literature (N-RGO [44], NAC-2 [67], TBC-K2.8 [19], A75-CTPW [9]).